nature communications

Article

https://doi.org/10.1038/s41467-025-64527-3

A dynamic biointerface in mussels mediated by a mechanoresponsive intermediate filament-based biopolymer

Received: 17 March 2025

Accepted: 17 September 2025

Published online: 28 October 2025

Check for updates

Lucia Youssef[1], Jenaes Sivasundarampillai[1], Emily N. P. Prowse[2], E. Deniz Eren[1], Franziska Jehle[1,3], Christopher Thibodeaux[1], Adam G. Hendricks[2], Daniel J. Jackson[4] & Matthew J. Harrington[1]

Mussels fabricate a distinctive biointerface that bridges their non-living biopolymeric byssus (used for anchoring in seashore habitats) with their soft-living tissue. Occurring in a region known as the byssus stem root, this biointerface is at once strong, yet also capable of on-demand release under apparent neurobiological control by the mussel, but this is not well understood. Here, we identify and sequence a previously unknown intermediate filament protein (MSP-1) that based on immunohistochemical staining and spectroscopic mapping comprises the surface of the stem root in direct contact with billions of motile cilia emerging from the living tissue. Further structural analysis indicates that MSP-1 is secreted as an α-helical coiled-coil but is mechanically converted subsequently to a β-sheet conformation. We posit that this mechanoresponsive conversion has a mechanical function in toughening the interface, but possibly also as a mechanosensory mechanism given its intimate contact with cilia in the living tissue.

Recent advances in bioimplants, including applications such as brain-machine interfaces, joint prostheses, and spinal fixations, aim to seamlessly integrate hard devices with soft biological tissues[1–4]. This integration is crucial for achieving both biocompatibility and functionality[1,5]. However, a significant challenge arises from the mismatch between these mechanically distinct materials[6]. At their interface, stresses concentrate, leading to structural failure that often takes the form of delamination in the contact zone, i.e., detachment of implants from the soft tissues[6]. Further complications may arise when these devices need to be removed or replaced once past their useful lifetime[7]. For instance, if dental implants need to be removed due to complications, such as bone loss and soft tissue recession[7], the process can trigger soft tissue collapse and lead to swelling and inflammation in the surrounding area[8]. Therefore, future bioimplant designs must consider both biointerface strength as well as the ability to detach safely and effectively without the need for complicated surgeries. Nature offers valuable insights that could guide the development of such advanced biointerfaces[6]. One prominent design paradigm that has received much attention is the use of functional gradients, which enable stable integration between distinct materials by avoiding stress concentrations through avoiding sharp interfaces[6]. Observed in the mantis shrimp dactyl club[9], squid beaks[10], tendon/ligament-to-bone connections[11], and marine mussel byssus[12], these systems avoid stress concentration through smooth transition in composition and/or structural hierarchy between mechanically distinct regions.

While effective at strengthening potentially weak interfaces, functional gradients do not solve the problem of on-demand release of the interface. In contrast, it was recently discovered that marine mussels (*Mytilus edulis*) have evolved a strong biointerface between living extracellular matrix comprising the soft tissue of the organism and a stiff non-living biopolymeric holdfast known as the byssus, which can be released on-demand by the mussel (Fig. 1)[13]. Mussels fabricate their protein-based byssus as a means of securely anchoring to hard substrates in wave-swept seashore habitats[14]. The byssus is comprised

[1]Department of Chemistry, McGill University, Montreal, QC, Canada. [2]Department of Bioengineering, McGill University, Montreal, QC, Canada. [3]Department of Biomaterials, Max Planck Institute of Colloids and Interfaces, Golm, Germany. [4]Department of Geobiology, Georg-August University of Göttingen, Göttingen, Germany. e-mail: matt.harrington@mcgill.ca

https://doi.org/10.1038/s41467-025-64527-3

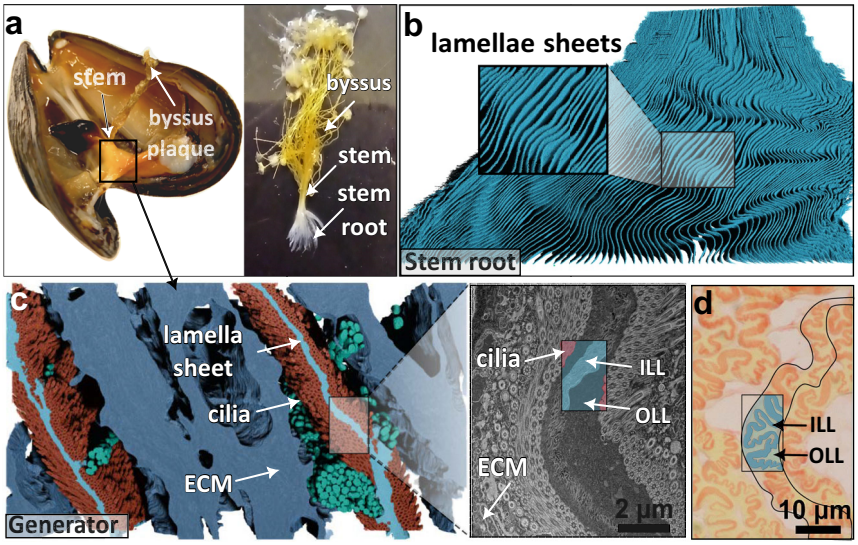

Fig. 1 | Overview of mussel byssus stem root biointerface. a An opened mussel with the stem pulled out (right), exposing the stem root that was embedded in the generator tissue. **b** False-colored 3D reconstruction of the PCE-µCT dataset of the lamellae in the generator, showing a zoomed-in image of the lamellar sheets. **c** A reconstructed 3D FIB-SEM image stack shows the structural features present in the generator tissue, highlighted in (**a**). The image on the right shows a high-magnification STEM image of the biphasic lamella in contact with the cilia, corresponding to the highlighted area in (**c**). **d** A section of the released stem stained with Sirius red, showing the biphasic composition of collagenous (ILL) and non-collagenous components (OLL) of the lamellae. **b**–**d** reproduced with permission from Sivasundarampillai et al., *Science*, **10.1126/science.adi7401** 2023, AAAS[16].

of numerous tough and adhesive fibers that converge at the byssus stem like branches attached to a tree trunk (Fig. 1)[14,15]. The stem is anchored securely into the living tissue at its base (the stem root)[15,16]. Remarkably, however, despite the very strong connection between the stem root and soft tissue, mussels can inexplicably jettison their entire byssus on demand in order to relocate or escape threats (Fig. 1a)[13,16]. This makes the mussel an ideal model system for studying a quick-release living/non-living bio-interface, which offers an exciting archetype for inspiring design of easily removable bioimplants. Yet, the mechanism of release is poorly understood.

The stem root consists of over 40 individual sheets, known as lamellae, each with a thickness of 2 to 3 microns and a distinct wavy morphology (Fig. 1b)[15,16]. The lamellae are interdigitated with the living tissue, creating a massive interfacial surface area in direct contact with nearly six billion cilia (Fig. 1c). Cilia movement, which is regulated neurobiologically with serotonin and dopamine, was shown to regulate the mechanical strength between the non-living and living tissue, thereby enabling byssus release on demand[16]. It is hypothesized that stem root release can be activated by a range of environmental factors, including physical, chemical, and mechanical stimuli[16], which points to the existence of a sophisticated sensory system that remains poorly understood.

Beyond the cellular pathways in the tissue, the role of the biopolymeric lamellar material of the stem root is also potentially critical, given its location at the juncture of the living and non-living. Notably, it was shown previously[15,16] that the lamella is biphasic in composition, consisting of a collagenous inner lamellar layer (ILL), staining positively for Sirius Red, and a non-collagenous outer lamellar layer (OLL), that does not, and which is in direct contact with the cilia (Fig. 1c, d)[16]. While the ILL is comprised of byssal collagens similar to those that comprise the core of the byssal threads, the composition of the OLL remains unknown. This poses important questions regarding its potential role, particularly given its position surrounding the collagenous ILL, which is already highly effective at mitigating mechanical stress based on its similarity to the byssal thread collagenous core.

In this work, we investigated the OLL composition, structure, and function employing a cross-disciplinary approach bridging cell biology, biochemistry, and materials science. In doing so, we identify a previously unknown protein called MSP-1, which has strong similarities to an important class of alpha helical coiled-coil (CC) proteins known as intermediate filaments (IF) that includes keratin, vimentin, and lamin. MSP-1 is secreted from vesicles stored within the living tissue surrounding the stem root, forming the fibrous outer layer of the stem root lamellae. While initially alpha helical in nature, the MSP-1 proteins in the OLL can be mechanically converted into β-sheet conformation. This may play a role in toughening the biointerface, but possibly also in mechanosensing by the mussel, although this remains to be verified experimentally.

Results

Protein extraction and analysis

Previous investigations of the byssus stem biointerface from distantly related mussels from the *Atrina* genus indicated the presence of a protein bridge between the tissue and byssus based on sugar and metal-binding[17]. Thus, to better understand the stem biointerface in *Mytilus edulis*, we performed a protein extraction to determine if there might be an analogous interfacial protein (Fig. 2). Proteins were extracted from a cleanly released byssus stem root lamellae using 5% acetic acid containing 4 M urea and 2 M thiourea using a tissue grinder resulting in the release of very small quantities of protein requiring silver staining to observe with SDS-PAGE (Fig. 2a). Nonetheless, every extract consistently showed the presence of a prominent band running slightly below the 70 kDa MW standard.

To identify the protein, the extract was digested with trypsin, followed by tandem mass spectrometry (MS/MS) analysis using gland-specific transcriptomes from *Mytilus edulis*. The top hit was a 66.9 kDa transcript, which showed 45% coverage by 23 unique tryptic peptides (Supplementary Fig. 1). Importantly, the transcript appears to be almost exclusively expressed in the stem generator gland of the mussel foot and was not prominent in any of the other secretory gland transcriptomes. The complete sequence, which was verified with 3′ and 5′ rapid amplification of cDNA ends (RACE), is provided in Fig. 2e. The protein consists of 584 amino acids, with an elevated molar concentration of serine (10.1 mol%), and combined asparagine and glutamine concentration of 11 mol%, with a notable presence of glutamine doublets.

https://doi.org/10.1038/s41467-025-64527-3

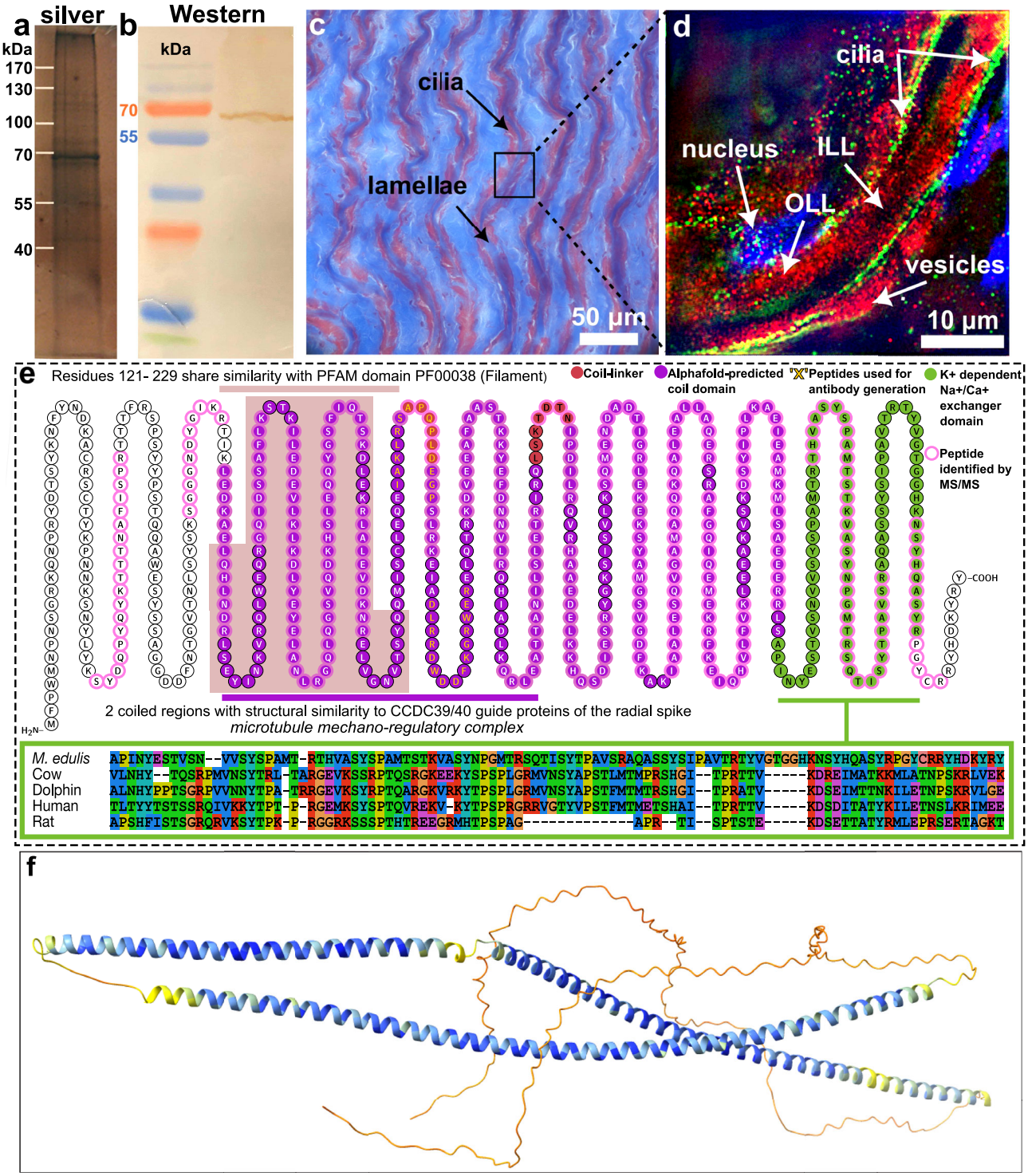

Fig. 2 | Extraction, sequence and localization of mussel stem protein-1 (MSP-1). **a** Silver staining of an SDS-polyacrylamide gel displays the band representing the protein extracted from the stem root lamellae ($N = 3$ gels from 3 specimens). **b** Western blot of the extracted protein stained in ($N = 2$ Western blots from 2 specimens) (**a**) using an antibody raised against MSP-1 peptide ($N = > 30$ images from 5 specimens). **c** Trichrome-stained section of the generator in which an unstretched stem root is embedded (blue: collagenous, red: non-collagenous components) ($N = > 30$ images from 5 specimens). **d** Immunostaining fluorescence image collected with SIM of a single stem root lamellar sheet and surrounding tissue; blue: nuclei, green: cilia, red: MSP-1 ($N = > 30$ images from 5 specimens). **e** A schematic of the protein sequence with annotations describing the characteristic features of MSP-1. **f** AlphaFold-predicted conformational structure of MSP-1. Source data are provided as a Source Data file.

Although this protein was extracted from the stem material, we could not detect a canonical signal peptide in our 5′ RACE data. To further verify that the protein sequence acquired corresponds to the protein extracted from the stem root material, we raised an antibody against two synthetic peptides selected from the protein sequence and performed a Western blot on the extracted protein (Fig. 2b). Both antibodies clearly react with the same ~70 kDa band observed with silver staining. This suggests this protein is secreted via a non-canonical pathway. In support of this, 2 paralogs of this protein-coding gene present in the *M. edulis* genome and an ortholog from *M. trossulus*

https://doi.org/10.1038/s41467-025-64527-3

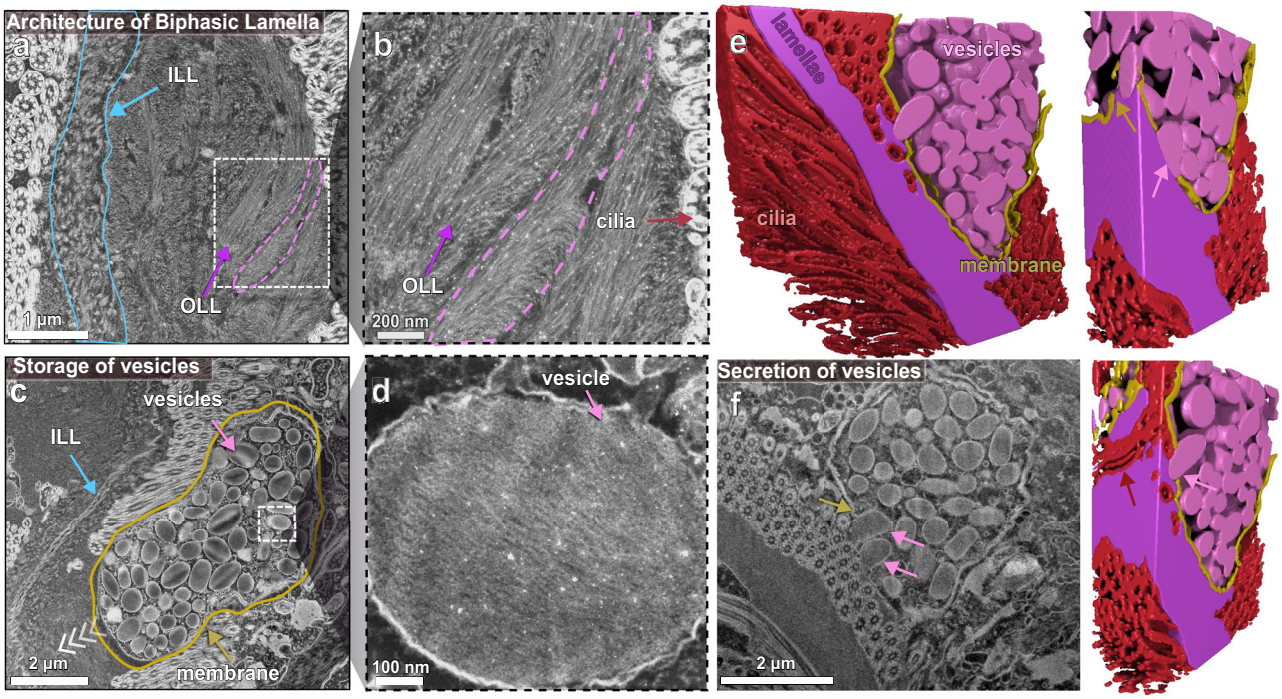

Fig. 3 | Electron microscopic characterization of stem root biointerface. a STEM image indicating the biphasic nature of the lamella in contact with the cilia. **b** Zoomed-in image of the region highlighted in (**a**), showing the OLL fibrils reorienting almost parallel to the cilia surface. The dashed pink outline in (**a**) and (**b**) indicate a region of the stem OLL that possibly originated from the contents of a single vesicle. **c** STEM image showing the concentration of vesicles at the interfaces prior to release. The yellow outline encloses a cluster of vesicles. (**d**) Zoomed-in image from (**c**) of a single vesicle consisting of IF fibrils (**a**–**d**: $N = > 50$ images from 2 specimens). **e** False-colored 3D model reconstructed from FIB-SEM image stack acquired from the generator. The colored arrows indicate the individual components in the 3D model. **f** Image from the FIB-SEM stack showing the fusion of the vesicles (pink arrow) with the membrane (yellow arrow) (**e**, **f**: $N = 3$ image stacks from 2 specimens).

also all lack signal peptides (Supporting Figs. 2 and 3). Given that the protein was extracted from the stem root, we name it mussel stem protein 1 (MSP-1).

Blasting the MSP-1 sequence against the protein database indicates a very strong similarity to numerous putative proteins with unknown function from a broad range of fresh and saltwater bivalves including other Mytilid mussel species, as well as various scallops and oyster species—suggesting a strong evolutionary conservation (Supplementary Figs. 2 and 3). While there is only weak sequence homology to other proteins with known function, it is worth noting that the C-terminal region shows some similarity to sodium-calcium exchanger (NCX) domains—a transmembrane protein that functions to exchange sodium (Na^+) for calcium ions (Ca^{2+}) across the plasma membrane[18]. Furthermore, a region closer to the N-terminus shows sequence similarity to domain IPR03900 in the InterPro database, an IF protein family[19]—a class of structural CC proteins that includes keratins, vimentin, and lamin—a mechanosensory nuclear envelope protein.

In support of this finding, a structural analysis using AlphaFold3 predicts that the protein possesses three alpha helical regions with two small non-helical linker regions between them and longer non-helical domains at both the N- and C-termini[20] (Supplementary Fig. 4), which was further supported by dedicated bioinformatic CC prediction algorithms (Waggawagga)[21]. All algorithms used further predict that MSP-1 will form a homodimeric alpha helical CC structure in the central region of the protein (Fig. 2f). Notably, these structural features (i.e., three helical CCs divided by non-helical linkers with unstructured termini) are highly characteristic of IF proteins[19,22,23]. Importantly, across this broad class of IF proteins there is relatively low sequence similarity despite the conserved structure. However, searching the AlphaFold3-predicted structure against the VAST protein structural database revealed similarity with certain IF proteins, in particular CCDC39/40, which binds to microtubules in cilia[24]. This suggests that MSP-1 is an IF-like protein with a homodimeric CC conformation.

Immunochemical localization

Given the proximity of cilia to the stem root lamellae and the finding of structural homology to CCDC39/40, it was essential to verify that MSP-1 was not an extraction artifact from the cilia. To confirm the localization of MSP-1, we used immunohistochemical labelling with structurally illuminated microscopy (SIM) employing an antibody raised against the alpha helical region of MSP-1. Cryo-sections of the native generator tissue were co-stained with the MSP-1 antibody, as well as antibodies for α-tubulin (for staining cilia) and DAPI (for staining cell nuclei) (Fig. 2d). Structured illumination microscopy (SIM) of stained generator tissue containing the lamella shows a strong staining of the lamella with the MSP-1 antibody, which is clearly distinct from the surrounding cilia, with nuclei clearly visible on the other side of the cilia (i.e., within the living tissue). Notably, the MSP-1 antibody is largely absent from the central region of the lamellar sheet, which is consistent with the collagenous composition of the stem root ILL determined with other methods. In addition, positive staining with the MSP-1 antibody is observed in the living septa tissue directly surrounding the lamella, consistent with the previously observed location of the secretory vesicles that are used to make the stem (Fig. 1c). Based on these data, we propose that MSP-1 is indeed the precursor that comprises the non-collagenous OLL of the byssus stem root lamellae.

EM characterization of the outer phase and the associated secretory vesicles

To further investigate the non-collagenous OLL and the associated secretory vesicles at higher resolution, we utilized various modes of electron microscopy (Fig. 3). Using scanning transmission electron microscopy (STEM), we observed that the outer phase of lamellae

https://doi.org/10.1038/s41467-025-64527-3

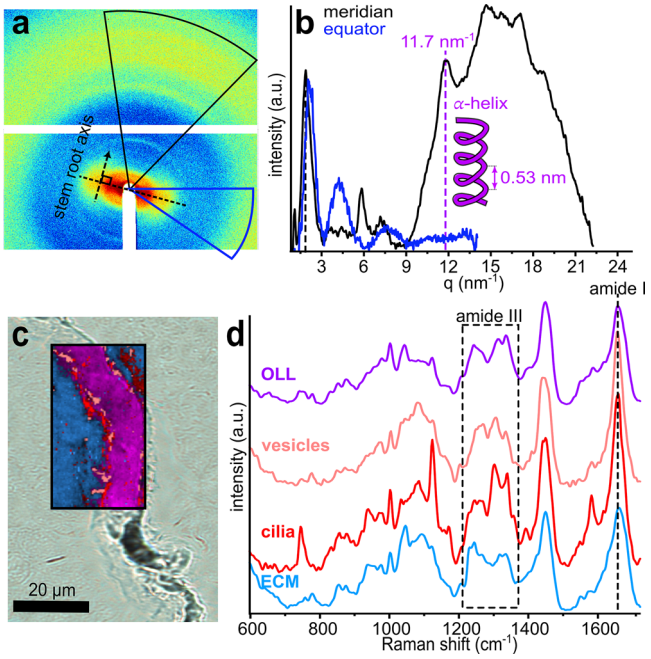

Fig. 4 | Conformational characterization of mussel byssus stem root outer lamellar layer (OLL). a WAXD diffractogram of the stem root. **b** Radial intensity profiles of (**a**) as a function of the scattering vector q from the meridional (black) and equatorial (blue) axes with respect to the stem root axis (**a**, **b**: $N = 4$ from 4 specimens). The illustration shows the alpha helical pitch corresponding to the peak at $q = 11.7$ nm^{-1} ($d = 0.53$ nm). **c** Raman image map of an unstretched stem root, showing the composition of the identified components in the spectra shown in (**d**) (**c**, **d**: $N = 4$ from 4 specimens). Source data are provided as a Source Data file.

exhibits a woven texture of thin fibrils, while the core consists of thicker fibrils that are presumably collagenous in nature based on histological staining and Raman spectroscopy[16] (Fig. 3a). The thin fibrils of the OLL are in direct contact with the cilia, molding their structure to the surface, and in many cases appearing to direct their end to be in contact with the cilia (Fig. 3b). While it is difficult to make out individual fibrils in the STEM images due to their highly packed organization, the shortest length fibrils at the edges are more than 100 nm, while the diameters appear uniform and in line with other IF fibers (~ 10 nm). Overall, the filaments are aligned along the axis of the stem lamellae. STEM imaging also reveals the presence of numerous secretory vesicles located at the periphery of the lamellae (Fig. 3c, d). While some vesicles have the rugby ball-like structure of the core vesicles, we observed numerous vesicles with a pill-like structure of the type II vesicles previously identified in the stem generator tissue[15] showing evidence of fibrillar contents, consistent with the OLL ultrastructure.

Focused ion beam scanning electron microscopy (FIB-SEM) is a powerful imaging modality that produces image stacks through micron-scale sample volumes with nanoscale resolution, which can yield 3-dimensional models through segmentation and reconstruction of principal features in the images. FIB-SEM reconstruction of the stem root biointerface also shows the pill-like morphology of the vesicles in 3D (Fig. 3e). Moreover, FIB-SEM reconstructions clearly show some vesicles whose contents are merging with the OLL between the cilia and sometimes, even entrapping the cilia within the newly formed OLL (Fig. 3 and Supplementary Movie 1). These data suggest that the MSP-1 secretion process is likely merocrine in nature, in which the vesicles fuse to the membrane and are secreted into the lumen (Fig. 3e, f), which is further supported by STEM images (Fig. 3c). This is also consistent with images from immunostained samples in which the vesicle contents appear to be secreted between the cilia. Interestingly, several STEM images show locally aligned fibrillar domains within the OLL that are on the same scale as the vesicles (1–2 μm), possibly supporting this assembly mechanism (Fig. 3a, b). Given this clear evidence that MSP-1 is secreted, the lack of signal peptide on the protein is unusual and suggests an unconventional protein secretion (UPS) pathway that does not involve the traditional transit from the endoplasmic reticulum through the Golgi apparatus[25]. Indeed, several other UPS pathways have been identified previously and consistent with our EM analysis, the IF protein vimentin has been shown in some cases to be secreted extracellularly via Type III UPS through the fusion of vesicles with the plasma membrane to release the protein cargo[26].

Protein conformation in the outer lamellar layer

Our findings suggest that the OLL consists of MSP-1 proteins arranged into fibrils similar in morphology to IFs, which would be expected to have an alpha helical CC conformation. To further investigate this hypothesis, we characterized protein conformation within the stem lamellae (Fig. 4). Wide angle X-ray diffraction (WAXD) of a cleanly released stem root reveals the presence of several distinct peaks superimposed onto a broad amorphous background peak (Fig. 4a, b). Notably, this method probes both the OLL and ILL of the stem root. Of particular relevance, we observe a prominent peak at $q = 11.7$ nm^{-1} (d spacing = 0.53 nm) which corresponds to the pitch of alpha helical secondary structure[27]. Notably, it is preferentially oriented along the long axis of the stem lamella, consistent with the STEM images that show the filaments in the OLL oriented along the long lamellar axis (Fig. 4c). Equatorial peaks appearing at lower q values ~ 4.5 nm^{-1} represent periodic spacing orthogonal to the stem root axis and are consistent with lateral packing of the coiled coils[28]. However, given the known presence of collagen fibrils in the ILL, which also have a similar lateral spacing[29,30], it is not possible to assign this peaks confidently.

Confocal Raman spectroscopic mapping investigation of the stem root biointerface shows that the lamella, as well as the secretory vesicles, show spectra that are consistent with an alpha helical conformation based on the presence of amide I peak maxima centered around 1655 cm^{-1} and amide III peak, which is higher at 1320 than at 1230 cm^{-1} (Fig. 4c, d)[31,32]. Given the resolution of this method, these spectra likely contain contributions from both the OLL and the ILL, so the fact that the alpha helical features are still evident is compelling. To complement the Raman-based measurements, ATR-FTIR were collected from a stem root that was gently extracted from the generator through serotonin-induced release, which was necessary as the resolution of FTIR microscopy would be insufficient to focus only on the lamella. ATR-FTIR spectra were collected using an evanescent polychromatic IR beam passed through a diamond crystalline probe pressed onto the sample. The acquired spectra will therefore be dominated by what is on the surface of the stem root (penetration depth of several microns), which should largely comprise the OLL. ATR-FTIR spectra show evidence for alpha helical structure based on presence of a component in the negative second derivative spectra at 1652 cm^{-1}—however, the spectra are largely dominated by an intense peak at 1626 cm^{-1} distinctive for the presence of beta sheet structure (plotting negative second derivative is a well-established analysis approach for identifying components in complex spectral bands in IR and Raman, such as the amide I)[32,33] (Fig. 5a, b).

It is important to mention here that to acquire a suitable signal with the ATR crystal, it was necessary to apply significant pressure onto the sample to establish tight contact. This leads to the generation of mechanical forces that, based on previous studies[32,34], are likely sufficient to convert the alpha helical structure of the OLL to a beta sheet conformation. This seems highly plausible given that mechanically activated alpha-to-beta conformational transitions have been reported in numerous materials based on IF CC proteins, including wool, vimentin filaments, whelk egg capsules, hagfish slime fibers, and, relevantly, freshwater mussel byssal threads from Dreissenid

https://doi.org/10.1038/s41467-025-64527-3

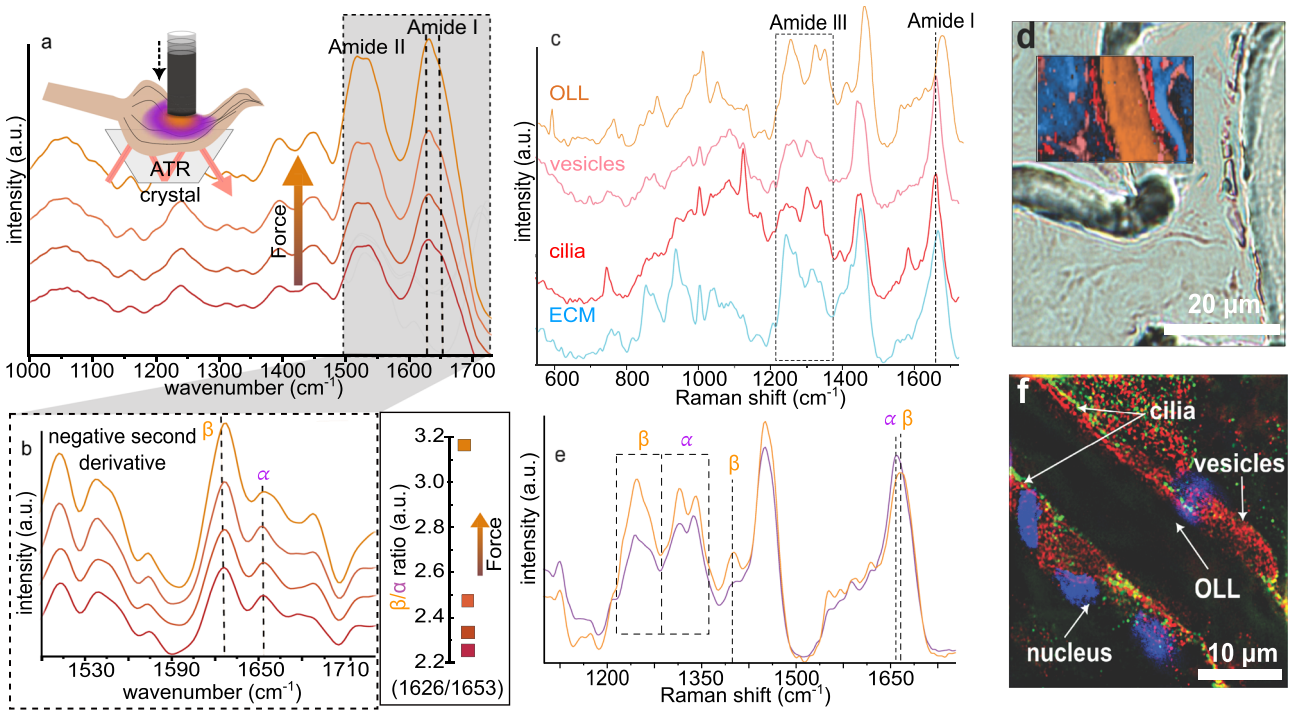

Fig. 5 | Mechanically induced alpha to beta conformational transition in the stem root OLL. a ATR-FTIR spectra acquired from the stem root as a function of the force applied by the ATR crystal. **b** Negative second derivative spectrum of the amide I band highlighted in (**a**), indicating the peaks corresponding to the beta sheet and alpha helix. The inset to the left shows the change in intensity of the ratio 1626 to 1653 cm^{-1} as a function of applied force (**a**, **b**: $N = 3$ from 3 specimens). **c** Raman spectra of a stretched stem root, with the localization of the components in the Raman map shown in (**d**). **e** Comparison between the Raman spectra acquired from a stretched (orange) versus unstretched root (purple): shift in the Amide I peak, increase in the intensity of the ~1400 cm^{-1} peak, and dominance of the beta sheet relative to the alpha helical conformation in the Amide III region after stretching (**c**–**e**: $N = 3$ from 3 specimens). **f** Immunostained section of a generator after the application of force to the stem root; blue: nuclei, green: cilia, red: MSP-1 ($N > 10$ images from 3 specimens). Source data are provided as a Source Data file.

mussels[31,32,35–38]. In further support of this hypothesis, we observed an increasing beta sheet content relative to the alpha helical content with increasing applied pressure indicated by the fact that the ratio of the negative second derivative peaks at 1626 cm^{-1} (beta) to 1653 cm^{-1} (alpha) increases by a factor of ~1.5. Considering that a significant force is already required to acquire the first measurement, we are likely already converting a large portion of the alpha helical structure by that point.

To further test this hypothesis, we measured Raman spectra from lamellae that experienced high mechanical forces through application of a sustained tensile stress to the byssus prior to measurement (Fig. 5c, d). Measurements clearly indicate that the spectrum changed compared to the unstretched samples, showing peaks consistent with an extended conformation (e.g., beta sheet) based on the shift of the amide I band to higher wavenumbers (from 1653 to 1665 cm^{-1}), the dominance of the 1230 cm^{-1} peak in the amide III band, and the appearance of a small peak at ~1400 cm^{-1} indicative of stretching of the alpha carbon bond in the protein backbone (Fig. 5e)[31]. In further support of the hypothesized alpha to beta transition, the MSP-1 antibody stops staining the lamella after mechanical forces have been applied to the stem although the secretory vesicles, which are enriched along the cilia-lamellar border, are still detectable in the surrounding tissue (Fig. 5f). This suggests that the mechanical transformation from alpha helical to beta sheet structure renders MSP-1 unrecognizable to the antibody, perhaps through formation of beta crystallites that sterically prevent access to the epitope[39]. This hypothesis is strengthened by the fact that the MSP-1 proteins within the secretory vesicles still stain strongly in these images—providing an effective internal positive control. Together, these findings strongly suggest that the alpha helical MSP-1 proteins within the OLL undergo a mechanically activated and lasting change into extended beta sheet structure. This seems biologically relevant given that the mussels experience constant mechanical loading at the seashore under the force of relentless crashing waves.

Discussion

This investigation has revealed the presence of an evolutionarily conserved protein—MSP-1—that comprises the outer layer of lamellae in the stem root of Mytilus mussels, and likely other bivalves from the oyster and scallop families based on conserved sequence homology. MSP-1 possesses prominent conformational features characteristic of the biologically important IF class of proteins. Yet, the lack of strong sequence level similarity with any of the currently identified classes (e.g., keratins, vimentins etc.), places it among the class VI orphan IFs[19]. As predicted by AlphaFold3, it possesses three dimeric CC regions linked by short non-helical sequences, as well as non-helical terminal domains—characteristic features of all IF proteins. Thus, this appears to be a unique IF protein evolved by bivalves for an unexpected function—coating the surface of a functionally distinctive bio-interface, unlike anything else reported in biology[16]. But what is the function of this protein since the collagenous core likely provides sufficient mechanical stability based on its spectroscopic similarity to the proximal byssus[16]?

The conversion of MSP-1 from alpha to extended beta-like structure might be an important aspect for understanding the role and function of this protein coating. From one perspective, the alpha to beta conversion will dissipate significant mechanical energy—computational modeling of deformation of the Lamin-network predicts a toughness that exceeds that of Kevlar[40]. This could be relevant given the role of the stem in dissipating energy from crashing waves—indeed every single byssus thread connects the stem root to the living tissue, an interface that is crucial for the survival of the mussel. However, as

mentioned, the byssal collagen core, is already incredibly tough (as tough as Kevlar) and extensible[41]. Furthermore, the alpha to beta transition, and thus the toughening effect, appears to be single-use, given that once it is converted it does not revert back to the alpha helical conformation. Thus, it seems excessive to add another protein layer if it only serves an identical purpose to the collagenous core, but less effectively. So, what might an alternative role be?

Given the previous studies of this dynamic, quick-release biointerface, it is interesting to consider that there might be a mechanosensory role of this alpha to beta conversion. MSP-1 is localized on the surface of the stem root lamellae, coating the collagen core and is situated directly at the living/non-living biointerface with the cilia. Furthermore, it is known that mussels are able to sense their mechanical environment and respond by either producing more threads or even by jettisoning their entire byssus and moving[13,42]. This sensing ability is biologically crucial, considering the high amount of energy invested in producing the byssus, which can reach up to 47% of the total metabolic budget in mussels, which produce threads daily[43]. Thus, the ability to "know" when to release and when to build more threads is vital to mussel survival and evolutionary fitness. Yet the mechanisms by which mussels make this decision are currently unknown. Perhaps the mechanoresponsive nature of the OLL plays a role. Indeed, precedence for IF CC proteins playing mechanosensory roles in cellular environments can be found in the lamins[44,45].

Lamins are type V IFs found in the nuclear envelope, where they function in mechanosensing and can impact gene expression[19,40,44,45]. The lamin meshwork is protected against mechanical forces through mechanisms integrated at every level of its hierarchical structure[40,44]. Under low mechanical loading forces, the reversible unfolding or sliding of the lamin CC domains helps absorb mechanical shocks and maintain the structural integrity of both the lamina and the nuclear contents[40,44]. When subjected to higher forces, however, an irreversible strain-induced stiffening occurs, enhancing filament stiffness, through an α-helix to β-sheet transition, further reinforcing the meshwork's resistance to failure[40,44]. This conversion is mechanically sensed through physical perturbations of cells and nuclei, facilitating the transmission of forces from the extracellular environment to the nucleus, which regulates chromatin organization, gene expression, and cell migration in both normal contexts, such as development and wound healing, and pathological contexts, such as cancer metastasis[44,46].

The parallels between lamin and MSP-1 are interesting, considering the role of mechanosensing in stem release and byssus production. It is intriguing to consider that sustained mechanical load placed on the byssus could mechanically convert MSP-1 from an alpha to beta conformation at the interface, which might be sensed by the mussel and provide essential information on how soundly the mussel is fastened to the surface, and whether new threads need to be laid down or whether the byssus needs to be released[16]. Given the intimate connection between the cilia and the OLL of the stem, and the well-established role of certain cilia in mechanosensing (e.g., in hearing, in kidney cells, in embryogenesis)[47–49], this is not entirely implausible. In this model, the mechanoresponsive conversion of MSP-1 is sensed, resulting in the release of neurotransmitters (e.g., serotonin) that initiate the beating of cilia and a quick-release of the stem[16]. Alternatively, if the cells can sense that MSP-1 is no longer being converted, it might signal that there is no longer a need to make more byssal threads, which are highly energy-intensive to fabricate[43]. This is relevant considering that mussels typically live in large sprawling clusters known as beds, in which mussels experience much larger forces on the surface of the bed than they do when protected on the inside of the cluster[13]. In principle, this could be a way for inner-cluster mussels to sense that they can stop making threads, thereby conserving resources. Numerous studies indicate that mussels regulate thread production based on mechanical factors[13], but the mechanism by which this is achieved remain unknown. While speculative, our discovery of MSP-1 offers an intriguing avenue for future transdisciplinary studies bridging cell biology, neurobiology, biochemistry, and materials science.

Interfacing living and non-living materials presents a significant engineering challenge due to the mechanical stresses generated at the interface and the complications arising during device removal. Mussels, however, have evolved a strong and easily releasable interface comprising cilia that intimately interact with the non-living byssus stem root lamellae. In this study, we identified a previously unknown protein, MSP-1, that comprises the outer lamellar surface, which exhibits structural similarities to IFs known for mechanically stabilizing intra- and extracellular structures[19]. MSP-1 undergoes a structural transition from an alpha helical CC to a beta sheet conformation—a change that provides mechanical toughness to the interface, but that might also enable mechanosensing pathways at the interface, given the intimate connection to billions of motile cilia. While the biochemical pathways underlying this putative mechanosensory process remain to be elucidated, this complex mechanical response provides valuable insights into designing multifunctional biointerfaces (e.g., implants, bioadhesives) capable of responding to external stimuli and on-demand release. Such systems could have broad implications for engineering adaptive and reversible interfaces in biomedical and industrial applications.

Methods

Materials

Adult blue mussels (*Mytilus edulis*) were sourced from Prince Edward Island and obtained from a local market. Mussels were acclimated and maintained in a recirculating tank system at 12–15 °C. The system used artificial seawater (Fluval Sea, USA) enriched with calcium, potassium, magnesium, and strontium to mimic natural marine conditions. Only adult specimens were used; sex was not determined, as it was not relevant to the study. Mussels were fastened to plexiglass using fishing lines and rubber bands, triggering them to produce fresh byssal threads within a few hours.

Histological imaging

For foot tissue analysis, samples were dissected, embedded in optimal cutting temperature medium (O.C.T.) within a mold, and rapidly frozen in liquid nitrogen-cooled isopentane. The frozen samples were cut into 5 µm sections with a CM1520 Leica cryostat at −20 °C. For staining with Sirius red, the sections were immersed in Bouin's solution for fixation overnight, followed by staining with 0.1% Sirius Red solution prepared in saturated Picric acid for 1 h. Subsequently, sections were rinsed twice with 1% acetic acid. Masson's trichrome staining was performed following the manufacturer's protocol (Thermo Fisher Scientific): initially, the sections were fixed in Bouin's solution overnight and rinsed with running tap water for 5 min. The fixed sections were then stained with Weigert's Iron Hematoxylin solution for 10 min, followed by another rinse in tap water. Afterwards, the sections were immersed in a phosphomolybdic-phosphotungstic acid solution for 10 min to exchange dye anions. Finally, the sections were stained with aniline blue solution for 5 min and rinsed with 1% acetic acid for a few minutes. Sections were images using a light microscope (Axio Scope.A1, Zeiss) equipped with a 6 megapixel CCD camera (Axiocam 505 color, Zeiss). More than 100 histological images were collected from at least 5 different individual mussel specimens.

Stem root protein extraction and characterization: To identify the protein composition in the stem root, the byssus stem was removed from the generator, and the lamellae roots were dissected away and ground up in a solution of 4 M urea and 2 M thiourea using a tissue grinder (10 roots in 150 microliter solution). The sample was centrifuged at 21,130 rcf at 4 °C for 10 minu using a Centrifuge 5424 (Eppendorf). Afterward, the supernatant was separated and mixed with 1× loading buffer. To denature the proteins, the resulting mixture was heated in boiling water for 5 min. The solubilized proteins (5 µl)

were then run on a 10% SDS-PAGE gel at 250 Amp/30 Vs for approximately 40 min at room temperature against the Spectra Multicolour High Range Protein Ladder (Thermo Scientific). Different gels of the same protein were stained with Silver Staining Plus Kit (Bio-Rad protocol) and subjected to western blotting using the generated antibodies against the stem root protein of weight 70 kDa. Protein extraction was performed four different times on stem roots extracted from four different specimens.

Mass spectrometry proteomics

To identify the protein components of the tryptic digest, which cleaves at the C-terminal side of arginine (R) and lysine (K), allowing for a maximum of one missed cleavage, from the 70 kDa protein excised from the silver-stained SDS-gel, liquid chromatography coupled with tandem mass spectrometry was employed. No fixed or variable modifications were specified. The lyophilized tryptic digest (80–540 ng) was reconstituted in 100 μL of 0.1% formic acid in water. A 20 μL aliquot of this solution was injected onto a Waters C18 BEH UPLC column (1.7 μm, 1 × 100 mm) and fractionated at a flow rate of 50 μL/min using a water/acetonitrile/formic acid solvent system. The gradient began with 97% solvent A (0.1% formic acid in water) and 3% solvent B (0.1% formic acid in acetonitrile), with solvent B increasing to 100% over 10 min. The column effluent was directed to the electrospray ionization source of a Waters Synapt G2-Si ion mobility mass spectrometer, where data were acquired in positive ion and resolution modes. Source settings included a capillary voltage of 3.0 kV, cone voltage of 40 V, source offset of 80 V, and desolvation temperature of 250 °C. Gas flow rates in the TriWave mass analyzer were: trap gas (Ar) at 2.20 mL/min, helium cell at 180 mL/min, and IMS gas flow (nitrogen) at 90 mL/min. Ion mobility separation was achieved with a travelling wave velocity of 1000 m/s and a wave height of 40 V at a nitrogen pressure of 3.2 mbar. Peptide ions underwent alternating cycles of low and high collision energy (0.4 s duration) in the TriWave's transfer region, for MS^e data acquisition. During the low energy cycle, the transfer collision energy was fixed at 5 V, while for the high energy cycle, it ramped from 25–55 V to induce collision-induced dissociation of precursor ions. Argon was used as the collision gas at a pressure of 0.03 mbar. The MS^e mode acquired precursor ion m/z values (MS spectra at low collision energy) alongside their fragment ion spectra (MSMS spectra at high collision energy). A Glu-1-fibrinopeptide B external lockmass standard was used to correct the acquired m/z values. The mass tolerance was set to 5.1 ppm for precursor ions and 12.8 ppm for fragment ions. Only peptides with a minimum length of six amino acids and at least three fragment ions were considered. In addition, no score cutoffs were applied, including for post-translational modification localization. Raw data were analyzed with Protein Lynx Global Server (PLGS, Waters Inc.) by matching spectra against the M. edulis transcriptome. The spectral search applied a false discovery rate of 4% and thresholds of 135 low-energy and 30 high-energy ion counts for detecting precursor and fragment ions, respectively. MS/MS proteomics was performed on stem root extracts from two different specimens. The identification software used was PLGS version 3.0.3. The experiment included one biological replicate.

Mussel foot gland transcriptome assembly

Six regions of the mussel foot tissue (core gland, cuticle gland, plaque gland, stem gland, mantle, and whole foot) were dissected from four individuals, preserved in RNA later, and shipped frozen to the University of Göttingen, Germany. Upon arrival, the samples were thawed and immediately placed in Qiazol (Qiagen #79306) for total RNA extraction, following the manufacturer's protocol. RNA quality was initially assessed by standard agarose gel electrophoresis and quantified using a Nanodrop. From the 53 highest-quality samples obtained from three individuals (representing three biological replicates), the best were selected and sent to the NIG sequencing center at the University of Göttingen for additional quality checks and library preparation. TruSeq mRNA libraries were constructed for both 50 bp single-end (SE) and 250 bp paired-end (PE) sequencing on the Illumina HiSeq2000 platform. The SE data were used to evaluate gene expression levels across all six tissues from the three biological replicates, while PE sequencing was carried out on pooled tissue types from the three individuals to assist with de novo transcriptome assembly (e.g., core gland samples from all three individuals were pooled and sequenced).

Before assembly, both SE and PE reads underwent multiple filtering steps. Initially, raw data files were processed using the command-line version of FastQC v.0.11.9 to assess overall data quality. Adapter sequences were removed using BBDuk from the BBTools package, with the default Illumina adapter file, a kmer of 25, and a minimum kmer length of 8. Reads were then quality-trimmed with Trimmomatic (version 0.36) before being error-corrected using Tadpole from the BBTools package with a kmer size of 50 bp. Potential rRNA contamination was removed using BBDuk and a ribo-kmer library derived from the Silva database. Finally, reads were filtered by length. After filtering, the data were processed again using FastQC v.0.11.9 to evaluate the impact of the filtering steps. Data was assembled using TransAbyss v2.0.1. Gene-specific primers were used to amplify overlapping 5′ and 3′ fragments of MSP-1 from RACE libraries which were subsequently cloned into pGEM-T (Promega) using standard TA-cloning methods. These cloned fragments were sequenced by standard Sanger chemistry. The protein sequence presented in Fig. 2e was generated using Protter[50] and the alignment using SeaView[51].

FIB-SEM

This approach was adapted from previous studies on mussel foot and generator tissue FIB-SEM analysis[16,52]. Briefly, the generator tissue was dissected from the mussel and excess water was removed by dabbing with Kimwipes. The sample was prefixed for 30 min at 4 °C in a solution of 3% glutaraldehyde, 1.5% paraformaldehyde, and 0.1 M cacodylate pH 7.2 buffer. After pre-fixation, the generator was cut into thin slices using a scalpel and fixed again in the solution described above for 2 h at 4 °C. The fixed sections were rinsed 5 times using the cacodylate buffer at 4 °C and then stained using 1% OsO4 for 1 h at 4 °C. Afterwards, the stained sections were rinsed again 3 times for 5 min each using the same solution as before, and then were dehydrated stepwise in different concentrations of acetone (50%, 70%, 90%, and 3 × 100%) for 1 h total. The dehydrated samples were then embedded in Epoxy (Epon 812 substitute Sigma-Aldrich, no 45359) and polymerized at 70 °C for approximately 2 days. The generator samples ($n = 2$) were initially polished to expose the tissue at the block surface. These polished blocks were then transferred to the Zeiss Crossbeam 540 (Carl Zeiss Microscopy GmbH, Germany), where a trench was milled into the surface using a 30 nA FIB current at a 30 kV acceleration voltage for SEM imaging. The sample was then polished using a 700 pA FIB probe at 30 kV. To remove thin slices of the sample serially, a 1.5 nA FIB current at 30 kV was used, with each slice measuring 20 nm in thickness. After each milling step, the sample was imaged using SEM, employing both secondary and backscattered electron detectors. The resulting images had a resolution of 2048 × 1536 pixels and a lateral pixel size of 20.61 nm. We collected five different FIB-SEM datasets from the generator tissue acquired from two mussel specimens.

The FIB-SEM dataset images were processed using Dragonfly software. Initially, the images were aligned using the sum of squared differences method, followed by manual correction of the alignment. A 3D convolution filter (size 3) was then applied to the image stack, and contrast enhancement was performed using the contrast-limited adaptive histogram equalization operation, with a kernel size of 100 and 256 bins. For 3D visualization of the generator, segmentation, and a deep learning algorithm were utilized in Dragonfly 4.1.

STEM

To examine the generator tissue at the nanoscale, scanning transmission electron microscopy (STEM) were conducted with a Thermo Scientific Talos F200X G2 S/TEM, equipped with a Ceta 16 M CMOS Camera, operated at a 200 kV acceleration voltage. Generator tissue was dissected from mussel feet following a previously established protocol[53], rinsed in cold water, and blotted to remove excess mucus. Samples were pre-fixed at 4 °C for 30 min in 3% glutaraldehyde, 1.5% paraformaldehyde, and 650 mM sucrose in 0.1 M cacodylate buffer (pH 7.2), then cut into thin cross-sections and fixed again for 2 h at 4 °C in the same buffer. After five rinses in cacodylate buffer, specimens were post-fixed with 1% osmium tetroxide (OsO_4) for 1 h at 4 °C. Osmium-free specimens were used for EDS analysis. Dehydration was performed in a graded ethanol series (50%, 70%, 90%, 3 × 100%, 10 min each at RT), and samples were embedded in epoxy resin (Epon 812 or Hard Plus 812, EMS #14115). Polymerization was performed at 65–70 °C for 48 h. Ultrathin sections (~ 100 nm) were cut using a PowerTome XL ultramicrotome and mounted on carbon-coated copper grids (200 mesh) for imaging. High-angle annular dark-field imaging was performed in STEM mode at magnifications of 16,500×, 46,000×, 66,000×, 130,000×, and 185,000×. Images were collected from stem generator samples collected from two different specimens.

Immunostaining and structured illumination microscopy (SIM)

Polyclonal antibodies were produced commercially by Genscript (Piscataway, New Jersey, USA) from rabbits using two selected peptides from the MSP-1 sequence as antigens (peptide 1: CAKLRSAPQPLDEGP and peptide 2: CLRRDREDFKGRWER). For immunostaining experiments, the antibody raised against peptide 1 was used since it produced a stronger signal.

Two conditions were tested for immunostaining experiments: with and without a force applied on the stem. In both conditions, the mussels were minimally cut open. In the former case, the stem was later pulled, yet not released, while in the latter, it was left intact. Directly after, the whole mussel was put in a beaker containing 4% PFA (in 1× PBS buffer) at 4 °C, overnight. Later, the generator tissue was dissected from the mussel and frozen in a mold containing an OCT medium (Neg 50). The frozen block was sectioned into 5 µm sections using a cryostat (Leica CM1520) and mounted on cover slips. The cover slips were functionalized with silica by immersing them in a solution of APTES/acetone (1:2 ratio) for 1 min, followed by a 1-min rinse in water.

In a petri dish, the coverslips, having the sections facing upwards, were covered with permeabilization buffer (1% Triton-×-100 in PBS) and incubated for 1 h on an orbital shaker at 60–80 rpm. In a new petri dish, enough blocking buffer (2% bovine serum albumin in PBS) was added to cover the sections and then incubated for 1 h on an orbital shaker at 60–80 rpm. Meanwhile, a humid chamber was prepared by taping a large piece of parafilm on top of an empty 1 mL tip box that contains water at the bottom. Once the blocking step is finished, 100 µL droplets of a solution containing the diluted primary antibody (MSP-1 synthesized antibody raised in rabbit, GenScript) and α-tubulin T9026 to mark cilia, raised in mouse, Millipore Sigma Catalogue # T6199 (1:400 in PBS) were pipetted per coverslip onto the parafilm and the coverslips were flipped face down onto the droplets using tweezers. The samples were incubated overnight at 4 °C.

Afterwards, the humid chamber was removed from the fridge and the coverslips were flipped faced up into a dish containing enough blocking buffer to cover the surface. The sections were incubated on an orbital shaker at 60–80 rpm for 5 min. The rinsing with the blocking buffer was repeated twice, where between each step the liquid was decanted from the dish into the sink. During the last wash step, a solution containing the diluted secondary Alexa 647 (Thermo Fisher Catalogue # A21244) anti-rabbit and Alexa 488 anti-mouse (Thermo Fisher Catalogue # A11001) (both 1:400 in PBS). 100 µL droplets of the prepared solution were pipetted per coverslip onto a new parafilm in the humid chamber and using tweezers the coverslips were flipped face down onto the droplets. The chamber was covered with an aluminum foil to protect the sample from light and left at room temperature for 1–2 h.

After the secondary antibody incubation, a new dish with PBS was prepared and the samples were washed 3 times with blocking buffer as previously done after the primary antibody incubation. Each dish was protected from light using aluminum foil. Next, 100 µL of 1 µg/mL DAPI in PBS were pipetted per coverslip onto a new parafilm in the humid chamber and using tweezers, the coverslips were flipped face down onto the droplets. The chamber was covered with an aluminum foil to protect the sample from light and left at room temperature for 20 min. Finally, the coverslips were put in a petri dish and washed with PBS.

To image the samples, the coverslips were mounted upside down on a microscope slide and sealed with grease to ensure the section stay hydrated after adding ~20 µL of PBS into the slides. A 100× oil objective with an immersion oil of having a refractive index of 1.56 was used to acquire images with the different excitation wavelengths (435, 528, and 683 nm) using the DeltaVision OMX Structured Illumination Microscope (SIM). The imaging was performed in sequential mode using a structural illumination light path. The optical section spacing was 0.125 µm within a sample thickness of 4 µm. The images were reconstructed in SoftWorks using the 3D beam reconstruction. SIMcheck[54] was used to determine the Weiner filter settings (Fig. 2f: 0.0187 (blue), 0.0197 (green), 0.203 (red); Fig. 5f: 0.0173 (blue), 0.203 (green), 0.020 (red)). We collected images from stained sections acquired from three different specimens, each for loaded and unloaded stem sample.

Confocal Raman spectroscopy

Raman spectra were acquired from 5 µm sections of the generator tissue, mounted on a microscope slide, using a linearly polarized laser ($\lambda = 532$ nm) operating around 7 mW with a confocal Raman microscope (Alpha 300 R, WITec). The spectra were collected with a 100× objective (NA = 0.9) and an integration time of 4 s. The Raman scattered light was detected by a thermoelectrically cooled CCD detector behind a 600 × *g*/mm grating. During the large area scan, a continuous scanning mode was used in True Surface mode to dynamically adjust autofocus in real-time, following the topography of the sample. The compositional maps were analyzed through projectFive WiTec software. The spectra were initially corrected by cosmic ray removal and background subtraction. Later, principal component analysis) was applied to identify the different components. We collected spectra from sections made from two different specimens, each for the loaded and unloaded conditions.

FTIR spectroscopy

ATR-FTIR studies were conducted on a FTIR Vertex 70 (Bruker), equipped with an ATR objective and a single-bounce diamond crystal. Each spectrum was acquired from over 100 scans using a HeNe laser, after running a background measurement. The absorbed IR light was measured using a DLaTGS detector at a spectral resolution of 4 cm^{-1}, covering a total range 4000 to 400 cm^{-1}. To conduct force-dependent measurement on the stem roots, a dried stem root was placed on the crystal at room temperature, and first spectra were acquired once the ATR crystal was pressed into the root until a recognizable signal appeared. The pressure was gradually increased by further tightening the screw, with additional spectra collected at each step. Data were collected using the Bruker Opus software and negative second derivative of obtained spectra were plotted using OriginPro software. Spectra were collected from two different specimens from three different locations on the stem root.

Wide angle X-ray diffraction

WAXD studies were conducted using an Anton Paar SAXSpoint 2.0 instrument. The radiation source is a CuKα (wavelength, λ = 1.5406 Å),

with a beam size of 0.58 mm × 0.36 mm and a 2D detector (Eiger R 1 M (Horizontal)). A slightly hydrated stem root was placed vertically (with respect to stem axes) in an enclosed tissue chamber to prevent dehydration and structural collapse under high operating vacuum conditions. The sample-to-detector distance for WAXD was 117 mm. X-ray exposure time for each sample was 30 min per frame for a total of 2 frames. Analysis of diffractions data was done on SAXS analysis software (Anton Paar). Data were acquired from two different stem root specimens.

Ethical statement

This research complies with all relevant ethical regulations for testing and research of *Mytilus edulis* in Canada.

Reporting summary

Further information on research design is available in the Nature Portfolio Reporting Summary linked to this article.

Data availability

All relevant data generated or analyzed during this study are included in this published article, supplementary information files, and source data files. Transcriptomic data are available on the NIH BioProject Database with project number PRJNA1225934. Proteomic data acquired through mass spectrometry are available on the MassIVE database with project number MSV000097450. Protein sequence data is available on the Genbank Protein database with accession number PV367252. Source data are provided with this paper.

References

1. Wellman, S. M. et al. A materials roadmap to functional neural interface design. *Adv. Funct. Mater.* **28**, 1701269 (2018).
2. Elnathan, R. et al. Biointerface design for vertical nanoprobes. *Nat. Rev. Mater.* **7**, 953–973 (2022).
3. Fang, Y. et al. Dissecting biological and synthetic soft–hard interfaces for tissue-like systems. *Chem. Rev.* **122**, 5233–5276 (2022).
4. Tibbitt, M. W., Rodell, C. B., Burdick, J. A. & Anseth, K. S. Progress in material design for biomedical applications. *Proc. Natl. Acad. Sci. USA* **112**, 14444–14451 (2015).
5. Wang, X. et al. Bioadhesive and conductive hydrogel-integrated brain-machine interfaces for conformal and immune-evasive contact with brain tissue. *Matter* **5**, 1204–1223 (2022).
6. Liu, Z., Meyers, M. A., Zhang, Z. & Ritchie, R. O. Functional gradients and heterogeneities in biological materials: design principles, functions, and bioinspired applications. *Prog. Mater. Sci.* **88**, 467–498 (2017).
7. Adler, L., Buhlin, K. & Jansson, L. Survival and complications: a 9- to 15-year retrospective follow-up of dental implant therapy. *J. Oral. Rehabil.* **47**, 67–77 (2020).
8. Berglundh, T., Persson, L. & Klinge, B. A systematic review of the incidence of biological and technical complications in implant dentistry reported in prospective longitudinal studies of at least 5 years. *J. Clin. Periodontol.* **29**, 197–212 (2002).
9. Amini, S. et al. A diecast mineralization process forms the tough mantis shrimp dactyl club. *Proc. Natl. Acad. Sci. USA* **116**, 8685–8692 (2019).
10. Miserez, A., Schneberk, T., Sun, C., Zok, F. W. & Waite, J. H. The transition from stiff to compliant materials in squid beaks. *Science* **319**, 1816–1819 (2008).
11. Rossetti, L. et al. The microstructure and micromechanics of the tendon–bone insertion. *Nat. Mater.* **16**, 664–670 (2017).
12. Youssef, L., Renner-Rao, M., Eren, E. D., Jehle, F. & Harrington, M. J. Fabrication of tunable mechanical gradients by mussels via bottom-up self-assembly of collagenous precursors. *ACS Nano* **17**, 2294–2305 (2023).
13. Carrington, E., Waite, J. H., Sara, G. & Sebens, K. P. Mussels as a model system for integrative ecomechanics. *Annu. Rev. Mar. Sci.* **7**, 443–469 (2015).
14. Waite, J. H. & Harrington, M. J. Following the thread: Mytilus mussel byssus as an inspired multi-functional biomaterial. *Can. J. Chem.* **100**, 197–211 (2021).
15. Tamarin, A. An ultrastructural study of byssus stem formation in Mytilus californianus. *J. Morphol.* **145**, 151–177 (1975).
16. Sivasundarampillai, J. et al. A strong quick-release biointerface in mussels mediated by serotonergic cilia-based adhesion. *Science* **382**, 829–834 (2023).
17. Yoo, H. Y. et al. Sugary interfaces mitigate contact damage where stiff meets soft. *Nat. Commun.* **7**, 11923 (2016).
18. Xue, J. et al. Structural mechanisms of the human cardiac sodium-calcium exchanger NCX1. *Nat. Commun.* **14**, 6181 (2023).
19. Dutour-Provenzano, G. & Etienne-Manneville, S. Intermediate filaments. *Curr. Biol.* **31**, R522–R529 (2021).
20. Jumper, J. et al. Highly accurate protein structure prediction with alphafold. *Nature* **596**, 583–589 (2021).
21. Simm, D., Hatje, K. & Kollmar, M. Waggawagga: comparative visualization of coiled-coil predictions and detection of stable single α-helices (sah domains). *Bioinformatics* **31**, 767–769 (2015).
22. Strelkov, S. V., Herrmann, H. & Aebi, U. Molecular architecture of intermediate filaments. *BioEssays* **25**, 243–251 (2003).
23. Chernyatina, A. A., Nicolet, S., Aebi, U., Herrmann, H. & Strelkov, S. V. Atomic structure of the vimentin central α-helical domain and its implications for intermediate filament assembly. *Proc. Natl. Acad. Sci. USA* **109**, 13620–13625 (2012).
24. Merveille, A. C. et al. Ccdc39 is required for assembly of inner dynein arms and the dynein regulatory complex and for normal ciliary motility in humans and dogs. *Nat. Genet.* **43**, 72–78 (2011).
25. Rabouille, C. Pathways of unconventional protein secretion. *Trends Cell Biol.* **27**, 230–240 (2017).
26. Parvanian, S., Coelho-Rato, L. S., Eriksson, J. E. & Patteson, A. E. The molecular biophysics of extracellular vimentin and its role in pathogen-host interactions. *Curr. Opin. Cell Biol.* **85**, 102233 (2023).
27. Pauling, L., Corey, R. B. & Branson, H. R. The structure of proteins: two hydrogen-bonded helical configurations of the polypeptide chain. *Proc. Natl. Acad. Sci. USA* **37**, 205–211 (1951).
28. Er Rafik, M., Doucet, J. & Briki, F. The intermediate filament architecture as determined by X-ray diffraction modeling of hard α-keratin. *Biophys. J.* **86**, 3893–3904 (2004).
29. Harrington, M. J., Gupta, H. S., Fratzl, P. & Waite, J. H. Collagen insulated from tensile damage by domains that unfold reversibly: in situ x-ray investigation of mechanical yield and damage repair in the mussel byssus. *J. Struct. Biol.* **167**, 47–54 (2009).
30. Krauss, S., Metzger, T. H., Fratzl, P. & Harrington, M. J. Self-repair of a biological fiber guided by an ordered elastic framework. *Biomacromolecules* **14**, 1520–1528 (2013).
31. Harrington, M. J. et al. Pseudoelastic behaviour of a natural material is achieved via reversible changes in protein backbone conformation. *J. R. Soc. Interface* **9**, 2911–2922 (2012).
32. Simmons, M. et al. Invasive mussels fashion silk-like byssus via mechanical processing of massive horizontally acquired coiled coils. *Proc. Natl. Acad. Sci. USA* **120**, e2311901120 (2023).
33. Yang, H., Yang, S., Kong, J., Dong, A. & Yu, S. Obtaining information about protein secondary structures in aqueous solution using Fourier transform IR spectroscopy. *Nat. Protoc.* **10**, 382–396 (2015).
34. Jafari, M. J. et al. Force-induced structural changes in spider silk fibers introduced by ATR-FTIR spectroscopy. *ACS Appl. Polym. Mater.* **5**, 9433–9444 (2023).
35. Zhmurov, A. et al. Mechanical transition from α-helical coiled coils to β-sheets in fibrin(ogen). *J. Am. Chem. Soc.* **134**, 20396–20402 (2012).

36. Fudge, D. S., Gardner, K. H., Forsyth, V. T. Riekel, C. & Gosline, J. M. The mechanical properties of hydrated intermediate filaments: insights from hagfish slime threads. *Biophys. J.* **85**, 2015–2027 (2003).
37. Kreplak, L., Doucet, J., Dumas, P. & Briki, F. New aspects of the α-helix to β-sheet transition in stretched hard α-keratin fibers. *Biophys. J.* **87**, 640–647 (2004).
38. Miserez, A. & Guerette, P. A. Phase transition-induced elasticity of α-helical bioelastomeric fibres and networks. *Chem. Soc. Rev.* **42**, 1973–1995 (2013).
39. Mortimer, G. M. & Minchin, R. F. Cryptic epitopes and functional diversity in extracellular proteins. *Int. J. Biochem. Cell Biol.* **81**, 112–120 (2016).
40. Sapra, K. T. et al. Nonlinear mechanics of lamin filaments and the meshwork topology build an emergent nuclear lamina. *Nat. Commun.* **11**, 6205 (2020).
41. Gosline, J. et al. Elastic proteins: biological roles and mechanical properties. *Philos. Trans. R. Soc. Lond. B Biol. Sci.* **357**, 121–132 (2002).
42. Côté, I. M. Effects of predatory crab effluent on byssus production in mussels. *J. Exp. Mar. Biol. Ecol.* **188**, 233–241 (1995).
43. Roberts, E. A. et al. Resource allocation to a structural biomaterial: induced production of byssal threads decreases growth of a marine mussel. *Funct. Ecol.* **35**, 1222–1239 (2021).
44. Vahabikashi, A., Adam, S. A., Medalia, O. & Goldman, R. D. Nuclear lamins: structure and function in mechanobiology. *APL Bioeng.* **6**, 011503 (2022).
45. Cho, S. et al. Mechanosensing by the lamina protects against nuclear rupture, DNA damage, and cell-cycle arrest. *Dev. Cell* **49**, 920–935.e925 (2019).
46. Danielsson, B. E. et al. Nuclear lamina strain states revealed by intermolecular force biosensor. *Nat. Commun.* **14**, 3867 (2023).
47. Djenoune, L. et al. Cilia function as calcium-mediated mechanosensors that instruct left-right asymmetry. *Science* **379**, 71–78 (2023).
48. van Megen, W. H. & Hoenderop, J. G. J. Bend or break: the primary cilium as a potential regulator of electrolyte reabsorption in the kidney. *Curr. Opin. Endocr. Metab. Res.* **34**, 100506 (2024).
49. Pan, B. et al. Tmc1 forms the pore of mechanosensory transduction channels in vertebrate inner ear hair cells. *Neuron* **99**, 736–753.e736 (2018).
50. Omasits, U., Ahrens, C. H., Müller, S. & Wollscheid, B. Protter: interactive protein feature visualization and integration with experimental proteomic data. *Bioinformatics* **30**, 884–886 (2014).
51. Gouy, M., Guindon, S. & Gascuel, O. Seaview version 4: a multiplatform graphical user interface for sequence alignment and phylogenetic tree building. *Mol. Biol. Evol.* **27**, 221–224 (2010).
52. Jehle, F. et al. Collagen pentablock copolymers form smectic liquid crystals as precursors for mussel byssus fabrication. *ACS Nano* **15**, 6829–6838 (2021).
53. Jehle, F. et al. Hierarchically-structured metalloprotein composite coatings biofabricated from co-existing condensed liquid phases. *Nat. Commun.* **11**, 862 (2020).
54. Ball, G. et al. Simcheck: a toolbox for successful super-resolution structured illumination microscopy. *Sci. Rep.* **5**, 15915 (2015).

Acknowledgements

We acknowledge use of the Facility for Electron Microscopy Research (FEMR) at McGill, support for X-ray diffraction studies from H. Titi at the McGill Chemistry Characterization (MC^2) Facility, and support for MS/MS proteomics from L. Taylor at the MUHC Proteomics and Molecular Analysis platform at McGill. We acknowledge Dr. G. Salinas-Riester and the team at the NIG in Göttingen for NGS sequencing and thank J. Stix for use of the ATR-FTIR microscope. M.J.H. was funded by Natural Sciences and Engineering Research Council of Canada (NSERC Discovery Grant RGPIN-2024-04221) and Canada Research Chair awards (CRC Tier 2 950-231953). D.J.J. was supported by a grant from the Deutsche Forschungsgemeinschaft (JA 2108/8-1 Project number 528314512). A.G.H. is supported by CIHR (PJT-185997) and NSERC (RGPIN/04608). F.J. was supported by the Max Planck Society. L.Y. was supported by an FRQNT Québec Merit fellowship.

Author contributions

L.Y. and M.J.H. conceived and designed the research project. L.Y., J.S., E.D.E., F.J., and D.J.J. performed the experiments. All authors analyzed and discussed the data. L.Y. and M.J.H. wrote the manuscript. All authors edited and commented on the manuscript.

Competing interests

The authors declare no competing interests.

Additional information

Supplementary information The online version contains supplementary material available at https://doi.org/10.1038/s41467-025-64527-3.

Correspondence and requests for materials should be addressed to Matthew J. Harrington.

Peer review information *Nature Communications* thanks Oguzhan Gunduz and the other anonymous reviewer(s) for their contribution to the peer review of this work. A peer review file is available.